Volumetric ultrasound localization microscopy with diverging cylindrical waves

Antoine Coudert, Arthur Chavignon, Louise Denis and Olivier Couture

***Abstract*— Transcranial ultrasound plays a limited role in neuroradiology due to its lack of resolution, planar imaging, and user-dependency. By breaching the diffraction limit using injected microbubbles, volumetric ultrasound localization microscopy (ULM) could help alleviate those issues. However, performing 3D ultrasound imaging at a high frame rate with sufficient signal-to-noise ratio to track individual microbubbles through the skull remains a challenge, especially with a portable scanner. In this study, we describe a ULM sequence suitable for volumetric transcranial imaging exploiting cylindrical emissions on multiplexed matrix probes, through simulations, hydrophone measurements, and flow phantoms. This geometry leads to a doubling of the peak acoustic pressure, up to 400 kPa, with respect to spherical emission and improved volume rate, up to 180 Hz. Cylindrical emissions also improve ULM saturation rate by 60% through a skull phantom. The assessment of microbubble velocity was also improved from 33% error in the average flow measured with spherical waves to a 5% error with cylindrical waves. Conversely, we demonstrate the detrimental impacts of cylindrical waves toward the field of view and isotropic sensitivity. Nevertheless, due to its enhanced signal-to-noise ratio and 3D nature, such a cylindrical volumetric sequence could be beneficial for ULM as a diagnostic tool in humans, especially when portability is a necessity.**

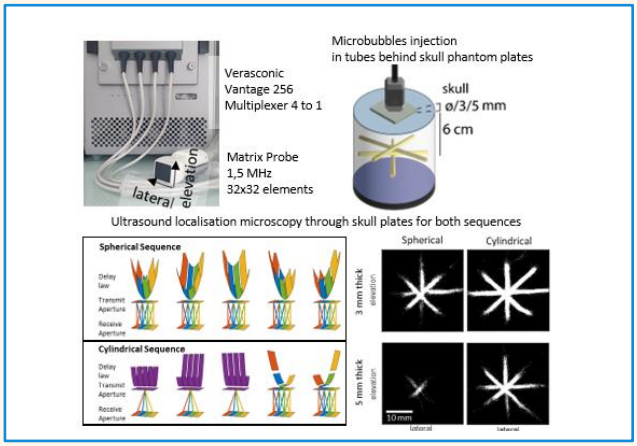

***Index Terms*—multiplexed probe, super-resolution ultrasound, transcranial ultrasound imaging, 3D ultrasound localization microscopy**

I. Introduction

THOUGH the brain represents just 2% of the body's mass, it consumes around 15% of the total cardiac output for blood supply [1]. Maintaining optimal blood flow to the brain is crucial for neuronal function and for preventing conditions like stroke, cancer, and dementia [2]. Traditional brain imaging techniques, such as MRI and CT scans, are often limited to hospitals, causing delays in diagnosing neurovascular diseases. A portable neuroimaging device could significantly speed up treatment in critical care, reducing mortality and morbidity[3].

Ultrasound imaging would allow such portability with the advantage of being non-ionizing, but its poor resolution hinders its capacity as a precise neuro-angiography tool. By bypassing the trade-off between resolution and penetration through the skull, ultrasound localization microscopy (ULM) has opened new possibilities to observe the smallest vessels in kidney [4], [5], liver [6], brain [7]–[11], both in humans and in animals [12]–[15].

To date, however, ULM has mainly been implemented as a microvascular 2D imaging modality by localizing individual microbubbles with subwavelength resolution. Although simpler, this dimensional deficit suffers from elevation projection artefacts and a lack of out-of-plane motion

Manuscript received December 28, 2023. This work was supported by the European Research Council through H2020 Program, ERC Consolidator Grants under Agreement 772786ResolveStroke. (Corresponding author: Antoine Coudert. (e-mail: antoine.coudert@sorbonne-universite.fr)

Antoine Coudert, Arthur Chavignon, Louise Denis and Olivier Couture are with the Sorbonne Université, CNRS, INSERM, Department Laboratoire d'Imagerie Biomedicale, France.

Olivier Couture is the holder of patents concerning super-resolution ultrasound imaging. He is also a co-founder and share-holder in the startup ResolveStroke. (e-mail: olivier.couture@sorbonne-universite.fr)

Highlights

- **This research explores cylindrical volumetric ultrasound, aiming to enhance signal-to-noise ratio and imaging volume-rate, potentially benefiting transcranial 3D ultrasound localization microscopy.**
- **The study indicates that cylindrical emissions in volumetric ultrasound imaging show promising improvements in microbubble detection and tracking through skull phantoms.**
- **This study's use of cylindrical emissions aims to address skull attenuation and expand the field of view, potentially contributing to enabling transcranial 3D ultrasound localization microscopy.**

correction. More importantly, 2D imaging is fundamentally limited by the medical expertise necessary during the selection of the plane, leading to a user-dependency detrimental to portable applications.

Volumetric ULM has been proposed and applied for small animal imaging [16], [17]. It is performed with a matrix array which detects ultrasound echoes from a large volume. Microbubble displacement are then tracked in a 3D volume, and can map vessels over a wide volume during a single bolus injection or a short vascular infusion of microbubble. Volumetric ULM creates new challenges as hundreds of millions of bubbles need to be tracked with sufficient precision within a few minutes. Hence, hundreds of volumes per second are necessary for this entire duration. In this context, fully-addressed systems, with electronic acquisition channels connected to each of the matrix elements, would provide the best volumetric high-frame rate. However, these electronic systems are currently far from portable[16], [18].

Ultrasound systems can be made smaller through the sparsity of the data acquisition. For volumetric ultrasound, matrix-sparsity [19], [20] or row-columns arrays were proposed [21], [22]. A simpler approach is the multiplexing of the acquisition between several panels, for instance N_{panels}=4 panels of 32x8 elements for a 1024 transducer matrix probe. By sequentially acquiring on each panel and accumulating the beamformed volumes, a full acquisition can be reconstructed. Unfortunately, with a multiplexer, a single volume image would require N_{panels} x N_{panels} pairs of emission-reception panel, reducing frame-rate by the same ratio. Moreover, emitting with a single panel each time reduces drastically the emitted acoustic intensity and, hence, the signal-to-noise ratio of the technique. A faster

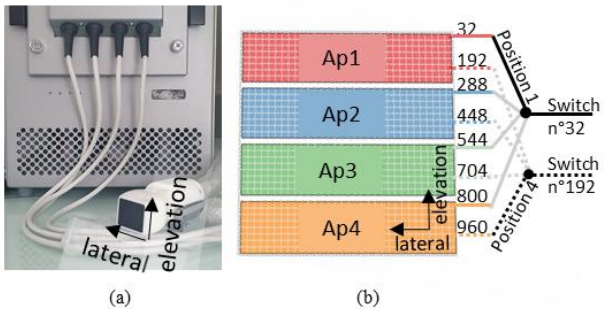

Fig. 1. (a). 1,5MHz matrix probe connected to a research ultrasound scanner. (b). Schematic view of panel composition with its 256 switches. The switch n°32 is in position 1 that's mean connected to element 32. The switch n'°32 is in position 4 that's mean connected to element 960

TABLE I
PARAMETERS

	Parameters	Values
Probe	Frequency	1.5 MHz
	Wavelength	0.9856 mm
	Bandwidth	60%
	Number of elements	1024
	Pitch	0.5mm
Pulse	Number of cycles	2
	Voltage	60V
Field II	Transducer frequency	1.5625 MHz
	Sampling frequency	12.5 MHz
	Speed of sound	1540 m/s
	Attenuation	0 dB/cm
	Number of cycles	2

"light" multiplexing version, which was demonstrated in stroke rat models, has been recently proposed, but it would difficult to apply on phased-array systems [23], [24].

The issues of frame rate and acoustical intensities become particularly pronounced for transcranial 3D ULM in humans. Some arteries are 6 cm deep in the brain, and the 3 to 5 mm thick temporal bone imposes an attenuation around 45 dB/cm at 2.25 MHz [25]–[28]. A lack of signal-to-noise ratio (SNR) would be worsened by the presence of the skull and by the divergence of the wave necessary to image a large sector of the human brain through the temporal window.

In this paper, we develop an acquisition sequence for a multiplexed phased matrix probe with a lower frequency (1.5 MHz) which could be used to perform 3D ULM through the human skull. We propose a new insonification method using cylindrical waves to preserve acoustical intensities. This exploits the capacity of some commercial multiplexers to connect the corresponding transducers on all panels for emission as long as the phase is common between these elements.

We compare these sequences to more traditional spherical emissions using simulations and experimental measurements [29]. Then, we measure imaging metrics, contrast-to-noise ratio and the geometry of the point-spread function, in different phantoms, without and with a skull phantom.

II. METHODS

A. Probe and electronics

High volume rate imaging was performed using a Vantage 256 (Verasonics, Kirkland, WA, USA) and a matrix probe

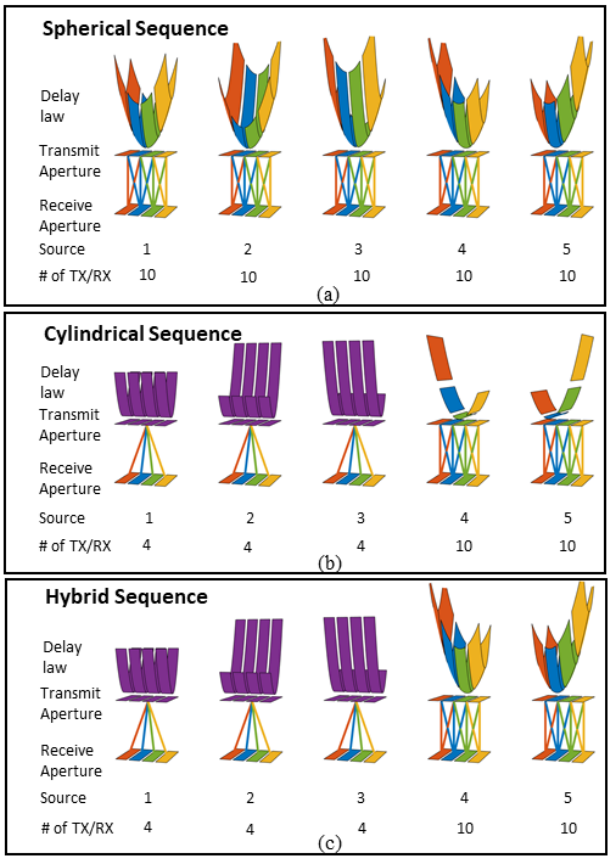

Fig. 2. Sequences' representations with Light combination. Each source delay law is represented for each sequence, (a). Spherical Sequence, (b). Cylindrical Sequence, (c). Hybrid Sequence, and the transmission/reception aperture couple done during the sequence is represented by a link. Red: emission with Panel 1 only, Blue: Panel 2, Green: Panel 3, Yellow: Panel 4, Purple: all panels. # of TX/RX: Number of emission-reception necessary for one virtual source volume.

centered at 1.5 MHz (Vermon, Tours, France) (Table 1). The probe was composed of 1024 elements of 500 µm pitch, aligned on a 32x35 grid. The 9th, 18th, and 27th lines were inactive and 300 µm wide, creating 4 independent panels assumed coplanar (Fig.1.a-b). The 1024 elements were connected to the 256 channels of the ultrasound scanner using a 4-to-1 multiplexer (Verasonics UTA 1024-MUX Adapter), which had 256 independent switches. Namely, the switch "i" was successively linked with elements "'i", "i+256", "i+512", and "i+768". A switch could change its position, allowing emission with one element and receiving with another from this list.

Additionally, emitting with the four connected elements at the same time was possible, as long as the emission waveform and delays were identical along the elevation axis. However, this approach was not allowed in reception. Four apertures were thus defined by the 256 consecutive channels for the 256 independent switches that corresponded to the four panels on the grid (Fig.1. b).

B. Spherical sequence

We defined the spherical sequence with five tilted spherical waves emitted in the medium for each combination with two panels. Spherical waves were generated by delay law from a virtual source 30-wavelengths behind the probe [28]. The five tilted spherical waves corresponded to azimuth and elevation shifts of {(0,0); (-5, 0); (5, 0); (0, -5); (0, 5)} degrees. Because of phase law, each spherical wave was decomposed into four parts corresponding to the four panels (Fig.2.a). We applied the light combination for the reception, corresponding to each aperture receiving its echo and those from the aperture of its direct neighbor's. It leads to a total of 10 emissions per virtual sources (Fig.2.a-Fig 3).

C. Cylindrical and hybrid sequence

Full cylindrical wave is defined as the combination of a diverging wave in the lateral direction with a plane wave in elevation. This allows a constant delay law on transducers aligned in the elevation direction. Therefore, the 4 panels could be connected together for the emission as the delays were similar in the elevation direction (Fig.2.b-c). To sample all transducers in this case, only 4 successive transmissions were required for the 4 reception apertures. (Fig.3)

Full cylindrical waves could only be induced when the angle is 0 in the azimuthal direction. In the other direction, waves still needed to be split in multiple emission-reception. Consequently, this sequence was still performed with ten emissions.

A third possibility was the hybridization of the cylindrical emission with spherical emissions as shown in Fig.2.c.

In general, framerate was computed according to the number of emissions needed to reconstruct a single volume. For

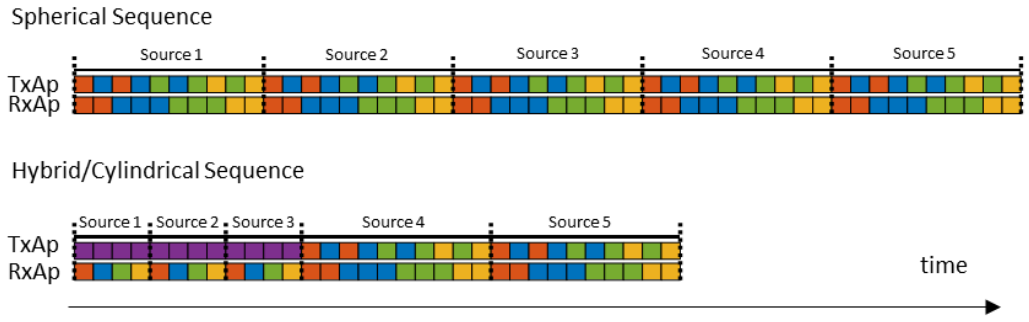

Fig. 3. Timeline of a frame for each sequence. Each color is associated to a panel used for emission or reception. (TxAp: Transmit aperture) or is receiving (RxAp: Receive Aperture). Red: Panel 1, Blue: Panel 2, Green: Panel 3, Yellow: Panel 4, Purple: all panels.

example, for spherical emissions, five virtual sources needed ten emissions each, leading to 50 emissions in total. For cylindrical emissions: there were four emissions per full cylindrical emission and ten per panel-per-panel cylindrical emission: leading to 32 emissions in total. Finally, for a hybrid emission, there were four emissions per full cylindrical emission and ten per panel-per-panel spherical emission, leading to 32 emissions as well. (Fig.3.)

D. Beamforming

Volume beamforming was realized in agreement with delay and sum beamforming [30]. We adjusted the forward delay in agreement with the kind of waves used. In case of spherical wave with a source (x_0, y_0, z_0) for a pixel (x_s, y_s, z_s), the transmit delay was defined by (1) with

$$D_{TX}(\boldsymbol{X}_s) = \sqrt{(z_s - z_0)^2 + (x_s - x_0)^2 + (y_s - y_0)^2} - \left(H\left(|x_0| - \frac{L_x}{2}\right)\left(|x_0| - \frac{L_x}{2}\right)^2 + H\left(|y_0| - \frac{L_y}{2}\right)\left(|y_0| - \frac{L_y}{2}\right)^2 + z_0^2 \right)^{\frac{1}{2}} \quad (1)$$

Where H is the Heaviside function, L_x and L_y are the length of the probe in x and y respectively. For cylindrical waves, the delay was modified in agreement with pixel localization. In front of the probe, cylindrical wave can be seen as a plane wave in one axis. Because of the limited size of the probe, the plane wave was limited. Outside of the probe perimeter, we assumed the wave to be spherical generated from the limit of the probe (2).

$$D_{TX}(\boldsymbol{X}_s) = \sqrt{(z_s - z_0)^2 + (x_s - x_0)^2 + H\left(|y_s| - \frac{L_y}{2}\right)\left(|y_s| - \frac{L_y}{2}\right)^2} - \sqrt{H\left(|x_0| - \frac{L_x}{2}\right)\left(|x_0| - \frac{L_x}{2}\right)^2 + z_0^2} \quad (2)$$

The receive distance D_{RX} was common to the different insonification sequences and corresponded to the spherical wavefront generated by the point scatterer as described in Perrot et al. [27].

E. Pressure field simulations

For each sequence, the pressure field generated by the probe was simulated with Field-II [31], [32]. A pulse propagation was simulated based on the specific delays necessary to generate the cylindrical, spherical or hybrid waves. Table 1 gathers all the simulation parameters. At 6 cm, acoustical amplitudes were measured on a flat grid of a size 110x110 pixels of 0.55x0.55 mm² each, collecting the peak-positive pressure in each point. Values were normalized by the maximum of a plane wave simulated to compare with calibration. The plane wave was defined by a source position 140 wavelengths behind the probe.

F. Pressure field measurements

The probe was fixed behind a Mylar window on the side of a tank filled with deionized water. It was coupled with acoustic gel (Fig 4.a). Each sequence was calibrated using a hydrophone needle, 0.2 mm in size (Precision Acoustic, Dorchester, United Kingdom), connected to an oscilloscope (Piscoscope 5444B, Pitcotech, United-Kingdom) and piloted by a computer. The hydrophone was fixed on a three-axes motor system and immersed in deionized water. The hydrophone travelled on a flat grid 110x110 mm in size with a one-wavelength pitch (0.95 mm). The grid was placed 60 mm away from the probe and centered on its axis. For each position, all sequences were emitted. The signal was acquired for each emission during 77,44 µs with a sampling frequency at 31.25 MHz. Maximum values of each position were normalized by the maximum obtained with a calibrated plane wave. The plane wave was defined by a virtual source position 140 wavelength behind the probe.

G. Spherical target

A 1mm diameter Tungsten carbide ball was placed in agarose 0.2% gel. The agarose phantom was placed on a 2-axis motor system. The probe was placed on the top of the gel, 6 cm away from the ball. All the setup (agarose phantom, gel and ball) moved together thanks to the 2-axis motor system. The ball was made to draw a 0.5 cm or a 1 cm radius circle around the axis of the probe with a step of 10 degrees (Fig.4.b). The three different sequences were performed at each position with 10 repetitions, and the point spread functions of the ball were measured. For each position and sequence, the ball was localized using gaussian fitting. The amplitude of the main lobe and the Full Width at Half Maximum (FWHM) were reported from the gaussian parameters. Side lobes in both axes were localized and the maximum amplitude was reported with the findpeaks Matlab (Mathworks, USA) function.

H. Ultrasound Localization Microscopy on vessel phantoms

A 2.3 mm diameter pipe coiled in a star-shaped tracks was plunged in 3% agar-agar gel (Fig.4.c). The probe was placed 6cm away from the star. Then, 1 µl of ultrasound contrast agent (Sonovue, Bracco, Italy) was mixed with 300 ml deionized water and was injected in the tube. Each sequence previously described was then tested to perform ULM. In this experiment, microbubbles were injected with a throughput of 12±2 mL/min corresponding of an average speed of 64mm/s or 25±2 mL/min corresponding of an average speed of 133mm/s. Each sequence was performed with and without a plate bone phantom (TruePhantom, Canada, 3 or 5 mm thickness, attenuation 45 dB/cm at 2.25 MHz) placed between the agar phantom and the probe.

A total of 48k volumes were acquired at 116 Hz frame rate for spherical sequence and 122 Hz or 179 Hz for cylindrical sequences and reconstructed with a delay-and-sum beamforming.

Microbubbles' signal was enhanced with a singular value decomposition filter by removing the first five singular values out of 200, corresponding to the number of images per series. Microbubbles were localized by three-dimensional radial symmetry [18]. Microbubbles with an amplitude of 9 dB with skull or 12.5 dB without skull above the surrounding noise floor were conserved and tracked by the Hungarian (simpletracker,

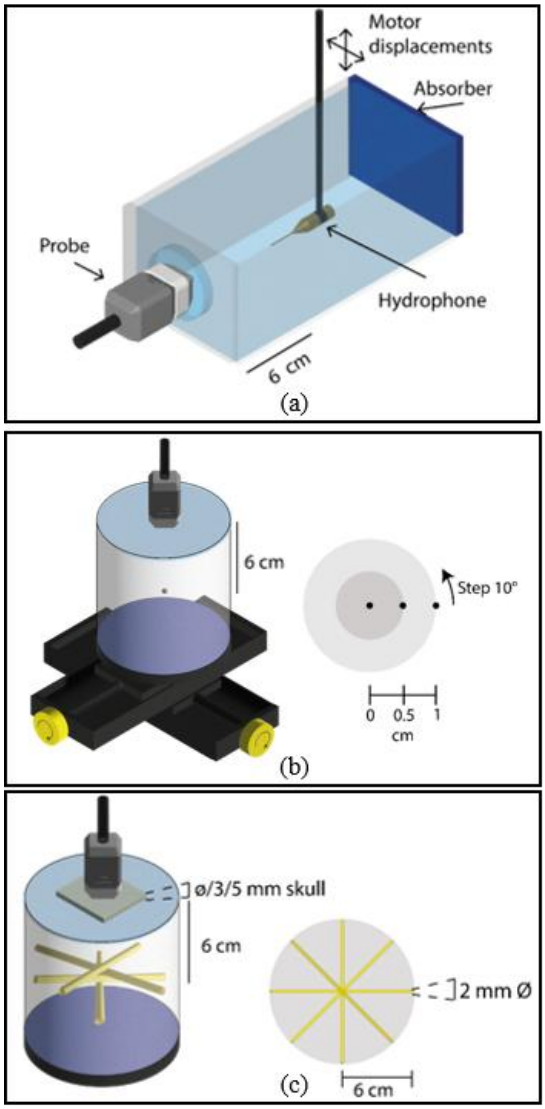

Fig. 4. (a). Calibration's setup. A hydrophone was immersed in a tank of deionized water. It measured the signal sent by the probe through a Mylar window. Two motors moved the hydrophone (b). Ball experimentation's set up. A ball was placed in an agarose phantom 6 cm away from the probe. The phantom was moved by two motors so as to make the ball follow two circles centered on probe position with radii of 5 mm and 1 cm respectively, in angular steps of 10°. (c). tube experimentation's set up. A 3% agar solution was poured around three connected latex pipes, which form a star, so that they were 6 cm from the surface. Water with microbubbles was introduced into the circuit. The surface probe imaged the medium either through a 3 or 5 mm flat skull phantom or without an aberrator.

Jean-Yves Tinenez) method with minimal persistence time of 5 frames and with a maximum pairing distance of 2 mm between 2 successive microbubble's positions.

Following the ULM reconstruction of each tubes, their length was measured with respect to the center of probe. The saturation of each ULM was computed by determining the ratio between the number of non-zeros pixel and the total number of pixels in the matrix.

III. Results

A. Pressure field comparison

The pressure field measured by hydrophone varied between different pulse-sequences (Fig.5). As expected, the spherical waves diverged in both directions. Meanwhile, the cylindrical waves only diverged in one direction and appeared plane in the other direction.

At 50 wavelengths, the cylindrical sequence resulted in a non-derated mechanical index (MI) of 0.67. Meanwhile, through a 3 mm skull, MI of the spherical sequence was 0.038, while the cylindrical sequence yielded 0.085.

We represented the measured intensity in the elevation-lateral plane on a logarithmic scale as compared to the intensity measured for a plane-wave emission. For source 1 (angles 0;0 degrees), cylindrical waves emitted by all panels appeared to reach a –6 dB signal with respect to the normalization of a plane-wave, corresponding to a 497 kPa pressure peak. Meanwhile, each emission of the decomposition by panel of the spherical waves reached a -20 dB, corresponding to a 190 kPa peak-pressure. For source 5 (0;5 degrees), the decomposition by panel of the cylindrical wave reached -12 dB or 400 kPa peak-pressure whereas spherical waves reached – 20 dB, i.e. 200 kPa, for the same source.

We also compared the intensity profile for one emission of each sequence with a Field-II simulation. The simulation seemed to have a higher signal than the hydrophone measurement. For instance, the spherical emission of source 5 reached a -12 dB in simulation while it is measured at -20 dB by the hydrophone (Fig 6.e-f).

B. Isolated scatter imaging

As a first approximation of the image quality, we determined the point-spread function of the imaging system from the echoes from a 1 mm steel ball in agarose (Fig 7.a). When the ball was in the central position, cylindrical sequence showed a higher amplitude than the spherical and hybrid sequence (Fig. 8.a). The shape of the point-spread function appeared similar

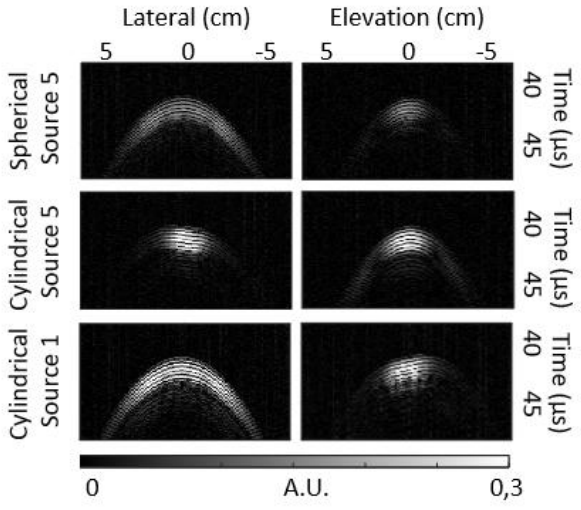

Fig. 5. Signals acquired by a hydrophone 6cm from the probe for three waves. First line: 1 panel emit source 5 of Spherical sequence. Second line: one panel emit source 5 of the cylindrical sequence. Third line: all panel emits source 1 of full cylindrical wave.

between sequence types, along with the side lobes (Fig 8.B).

To observe the anisotropy inherent to certain emission sequence, we moved the ball at 5 and 10 mm away from the transducer axis and then rotated the ball around the same axis. By cumulating the image intensity at each angle, separated by 10 degrees, we obtained a disk representing the inhomogeneities of the echoes depending on the ball positions. At 5 mm, the ball appeared uniform on all imaging sequence at each angle (Fig 7.b. Fig 8.b). However, 10 mm away from the transducer axis, the cylindrical and hybrid sequences showed a favorable direction (lateral) with respect to their sensitivity (Fig 7.c Fig 8.c). The spherical sequences appeared relatively constant, irrespective of the direction (Fig 7.b-c Fig 8.b-c).

The emission sequences also affected the amplitude of the side lobes, which can be visualized on the polar plots in Fig.8.b-c. There are two decades in amplitude difference between the side and main lobes. The angular variation of these sidelobes was more pronounced for the cylindrical and hybrid sequence with respect to the spherical approach, which appeared approximatively constant. (Fig 8.b-c).

C. ULM through skull phantom

We compared ULM obtained with the three difference sequences behind skull phantom plates with a thickness of 3 mm or 5 mm. Hybrid and cylindrical sequences could reach a volume rate of 179 Hz. However, for a better comparison, we limited their volume rate to be equivalent to that of the spherical

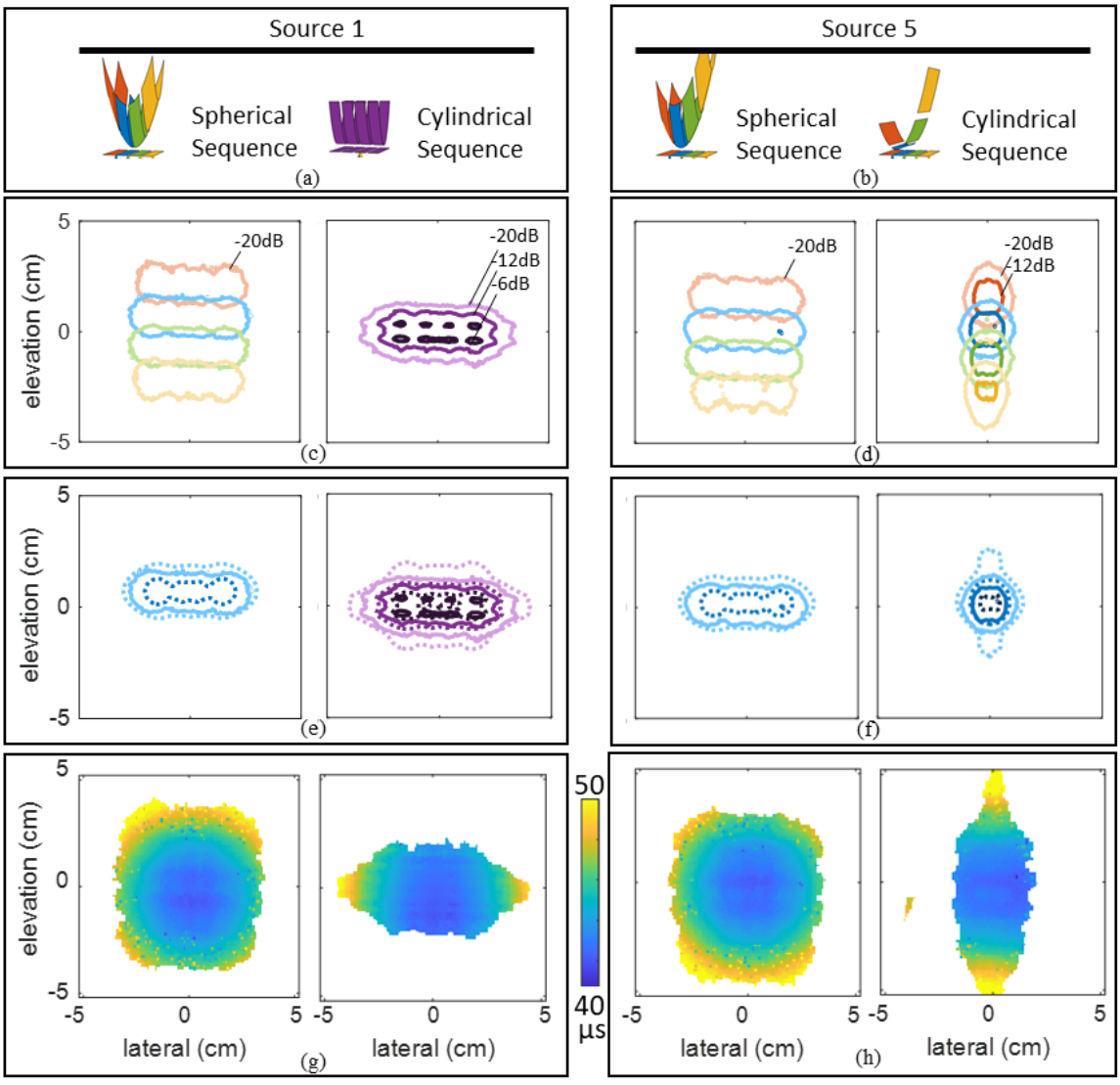

Fig. 6. (a). Delay law of source 1 for spherical and cylindrical sequence. (b). Delay law of source 1 for spherical and cylindrical sequence. (c). Contour plots for source 1. Signals were normalized by the maximum plane wave acquisition with a color corresponding to panels that emit. the four part of the wave for spherical sequence are superimposed. (d). Contour plots for source 1. Signals were normalized by the maximum plane wave acquisition with a color corresponding to panels that emit. the four parts of the wave for spherical sequence are superimposed. (e). Contour plots for source 1. Signals were normalized by the maximum plane wave acquisition with a color corresponding to panels that emit. Only one wave is represented (bold line) and compared with the simulation (dot line) computed on Field-II. (f). Contour plots for source 5. Signals were normalized by the maximum plane wave acquisition with a color corresponding to panels that emit. Only one wave is represented (bold line) and compared with the simulation (dot line) computed on Field-II. (g, h) Pulse arrival time in microseconds in an area with sufficient SNR (-28 dB)

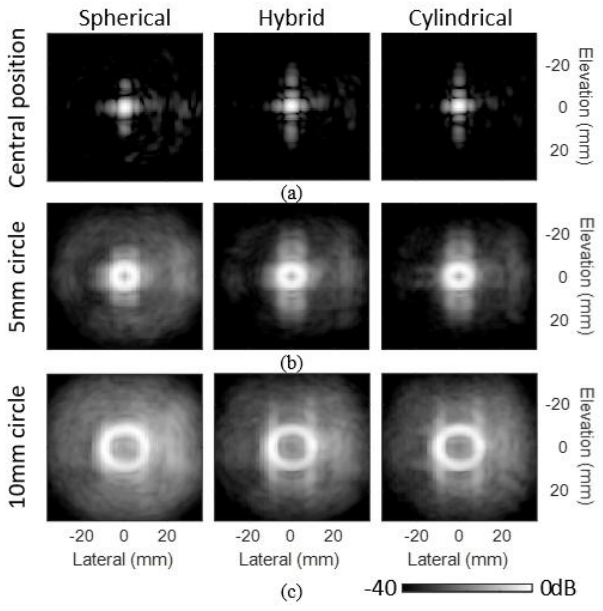

Fig. 7. Sequence comparison from a 1 mm spherical reflector. A: Axial projection of a volumetric B-mode at z = 6±1.5 cm with the reconstruction of each ball profile from a full emission sequence. (a). central position. (b). Rotating the bead in a circle of 5 mm radius around the transducer's main axis, (c). Circle of 10 mm radius. Each image has been normalized with its own maximum. The 40 dB dynamic range is common to all panels and represented in the bottom. Quantification is presented in Fig.8.

wave sequence (116 Hz for spherical sequence, 122 Hz for hybrid and cylindrical ones). Cylindrical and hybrid sequences showed a saturation 60% higher than that of the spherical sequences for the 3 mm-thick skull plate (Fig 9.a). A thicker skull plate showed less detectable microbubbles for the ULM process. This added attenuation impacted the spherical sequences in particular with an 89% loss in saturation with respect to a 70% diminution for the cylindrical sequences. (Fig 9.b).

The directionality of the cylindrical and hybrid sequences was again demonstrated by the length of observable tubing. The spherical sequence showed a uniform sensitivity across the angles, while the cylindrical sequences could extend the sensitivity to microbubbles in one direction.

D. Microbubbles flow measurements

We also measured the ability of the different sequences to follow microbubbles at flows of 12 ml/min and 25 ml/min. These experiments were performed without the skull plate. In the cases of the different insonifications, the microbubbles localizations were confined within the 2 mm diameter of the tube.

At a flow of 12±2 mL/min , the mean velocity reference value (64 mm/s) falls within 0.2 standard deviation of the mean microbubble velocity measured with all insonification methods (spherical, hybrid, cylindrical). However, at 25±2 mL/min, the spherical and low-frame-rate cylindrical methods were respectively 1.2 standard deviation and 0.8 standard deviation below the expected velocity (133 mm/s). Meanwhile, the expected value fell within 0.05 standard deviation of the 179

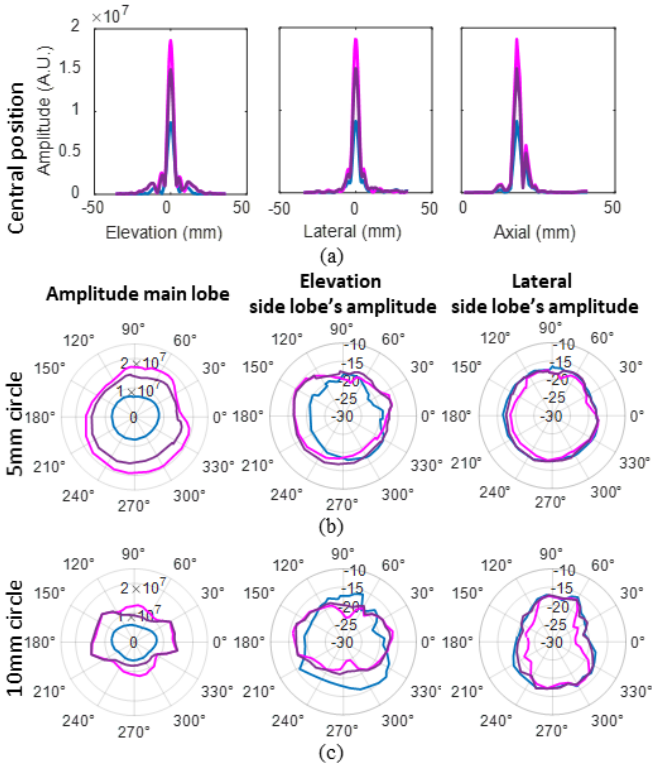

Fig. 8. (a). Point Spread function (PSF) analysis of the central point for each sequence: spherical sequence in blue, hybrid in purple, and cylindrical in pink. A. Amplitude of the central point depending on the lateral position (left). on the elevation position. (Middle), on the depth. (right) (b)-(c). Polar plot with intensity of the image of the rotating bead. (b). Circle of 5 mm, (c). Circle of 10 mm. First column: amplitude of the main lobe; Second column: amplitude of the elevation side lobes in dB according to main lobe; Third column: amplitude of the lateral side lobes in dB according to main lobe.

Hz frame rate cylindrical measurements. This phenomenon is confirmed by the presence of aliasing at the center of the vessel for the slowest volume rate at high flow which didn't exist at a low flow (Fig 10.c-d).

IV. Discussion

The goal of this study was to define new ultrafast sequences

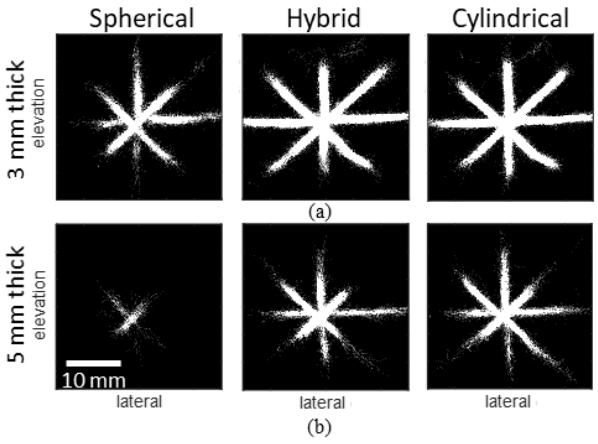

Fig. 9. (a). ULM comparison for a star-shaped track 6 cm away from the probe behind a skull phantom plate with a thickness of 3 mm (b). for 5 mm (attenuation: 45 dB/cm at 2.25 MHz).

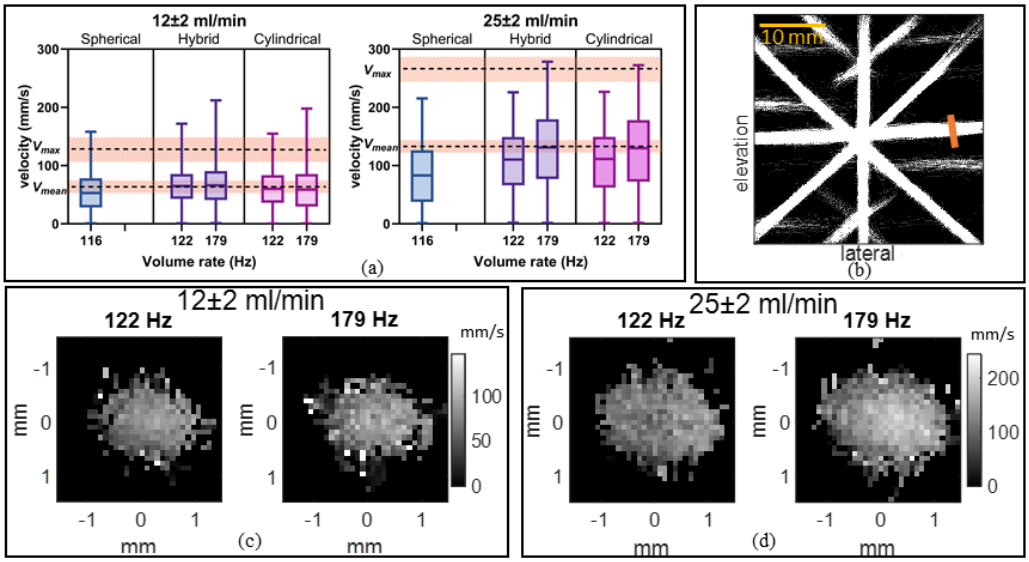

Fig. 10 (a). Velocity of bubbles found for 12 ml/min and 25 ml/min for each sequence and volume rate with theoretical mean velocity and theoretical maximum velocity. the area of uncertainty is in orange. (b). ULM using the hybrid sequence at a 179 Hz volume rate without a skull. The cross-section in Fig.9.c-d is obtained at the orange line. (c). Cross-section (1 mm thick) of the microbubble off-plane velocity for hybrid sequence at 2 volume rates 122 Hz and 179 Hz at 12 ml/min, (d). and at 25 ml/min. Error bars are extreme values.

to perform 3D Ultrasound Localization Microscopy across human skull bone phantom. The objective of the sequence was to alleviate the issues arising from bone attenuation and the necessity to image a large fraction of the human brain from the narrow temporal window. It was also important to achieve high volume rate in order to follow accurately the motion of microbubbles in different vessel calibers. Additionally, we wished to make the technique implementable on portable ultrasound systems which have a limited number of electronic channels (256 multiplexed 4 times).

The 32x32 elements transducers that we used had a center frequency of 1.5 MHz. We selected this frequency because ULM can bypass the traditional trade-off between resolution and penetration. Hence, a lower frequency than conventional transcranial Doppler could be selected in order to enhance the penetration of the acoustical wave through the skull.

Divergent spherical waves with virtual sources for ultrafast 3D imaging, as discussed in Provost et al [29]., represent the simplest geometry for emission and beamforming. As shown in the rotating shifted PSF, it also allows an isotropic insonification and point-spread-function. However, its overall acoustic pressure and, hence, signal-to-noise ratio was relatively low due to the divergence in two axes and the emission of only a single panel at once. This deficiency was demonstrated when ULM was performed through the thickest skull for which the spherical sequence was incapable of an appropriate reconstruction of the vessel phantom.

Spherical sequences necessitate acoustic pulses of different phases for each transducer of the matrix. Such electronic limitations imposed panel-by-panel emission, leading to 10 different emissions-reception for each spherical sources with only a fourth of the elements emitting each time. It restricted the frame-rate to 122 volume per second, inducing aliasing for the fastest flow studied.

Cylindrical waves were proposed for two reasons. Firstly, to restrict the divergence of the beam in only one axis. Secondly, to bypass the incapacity of the multiplexer to impose different emissions on groups of coupled elements between panels. Cylindrical emission, in one axis, allows an emission over all the connected panels. The main consequence is to increase the SNR due to an increase in acoustical pressure of the pulses. This allowed both cylindrical sequences to cross the thickest skull and yield an extended view of the vessels in the phantom. Moreover, the cylindrical sequences were able to achieve volume rates around 180 Hz, which prevented aliasing for the fastest flow rate (25 ml/min).

However, cylindrical waves were not isotropic. The rotating PSF experiment (Fig.7-8) and the ULM of the vessel phantom (Fig.9) showed a preferential direction which would need to be considered when the microbubble localization is performed in ULM. By the same token, side-lobes were also anisotropic for the cylindrical directions, leading to potential artefacts. These side-lobes were attenuated by the skull phantom and did not impact imaging in such conditions. However, as the ULM process relies on localization processes, such as Radial Symmetry, anisotropy could have an important impact on the localization precision in different directions.

In general, both hybrid and cylindrical sequences appeared to enhance SNR and volume-rate and seemed well adapted to simpler, and more portable, electronics than fully-addressed systems. Nonetheless, as this study was performed in-vitro and with simulation, the impact of the anisotropy and the increased side lobes in transcranial animal or human studies is difficult to predict. In particular, this newly introduced trade-off between SNR and artefacts should be tested in larger animals. However, we expect that higher SNR would increase the number of microbubbles that can be detected, and hence, improve the quality of transcranial ULM.

Several other emission sequences can be imagined with multiplexed matrix arrays. For instance, emissions with a limited number of transducers could be repeated to achieve higher frame rates, to the cost of a lower acoustical pressure.

The precise choices in the current studies are, hence, a subset of possibilities that we deemed optimal for transcranial ultrasound localization microscopy with diverging beams, in particular to optimize signal-to-noise ratio.

For future implementations, a fully-addressed emission and a multiplexed reception, might achieve a better compromise, since emission channels are simpler in their implementation than receive channels. However, in this context, the cylindrical sequences could still be used to enhance the signal-to-noise ratio. Additionally, further corrections to take into account transducer misplacement at fabrication could be taken into account to improve image quality [33].

In the future, using the sequences described in this study, transcranial 3D ULM could be achieved in humans, allowing neurovascular imaging with a portable ultrasound system.

We envision such scanner to be exploited for rapid stroke triage in ambulance or in intensive care units, reducing significantly the time-to-treatment and, in consequence, both morbidity and mortality.

V. Conclusion

In this article, we proposed the use of cylindrical emission sequences on matrix arrays to enhance the benefits of multiplexing and improve the signal-to-noise ratio in transcranial ultrasound imaging. Compared to conventional spherical sources, cylindrical sequences improved frame rate and microbubble detectability but also introduced anisotropic sidelobes. This innovative approach has the potential to advance ultrasound localization microscopy in humans, addressing current limitations caused by skull attenuation and beam divergence.

References

[1] C.-Y. Xing et al., “Distribution of cardiac output to the brain across the adult lifespan,” J Cereb Blood Flow Metab, vol. 37, no. 8, pp. 2848–2856, Aug. 2017, doi: 10.1177/0271678X16676826.

[2] C. Iadecola et al., “The Neurovasculome: Key Roles in Brain Health and Cognitive Impairment: A Scientific Statement From the American Heart Association/American Stroke Association”. Stroke.vol.54, no 6 e251-e271, June 2023, doi:10.1161/STR.0000000000000431

[3] K. Fassbender et al., “ Impact of mobile stroke units”, J Neurol Neurosurg Psychiatry, vol. 92, no 8, Art. no 8, Aug. 2021, doi: 10.1136/jnnp-2020-324005.

[4] S. B. Andersen et al., “Super-Resolution Imaging with Ultrasound for Visualization of the Renal Microvasculature in Rats Before and After Renal Ischemia: A Pilot Study”, Diagnostics, vol. 10, no 11, Art. no 11, nov. 2020, doi: 10.3390/diagnostics10110862.

[5] S. B. Andersen et al., “Evaluation of 2D super-resolution ultrasound imaging of the rat renal vasculature using ex vivo micro-computed tomography”, Sci Rep, vol. 11, no 1, p. 24335, dec. 2021, doi: 10.1038/s41598-021-03726-6.

[6] C. Huang et al., “Super-resolution ultrasound localization microscopy based on a high frame-rate clinical ultrasound scanner: an in-human feasibility study”, Phys. Med. Biol., vol. 66, no 8, p. 08NT01, apr. 2021, doi: 10.1088/1361-6560/abef45.

[7] V. Hingot et al., “Early Ultrafast Ultrasound Imaging of Cerebral Perfusion correlates with Ischemic Stroke outcomes and responses to treatment in Mice”, Theranostics, vol. 10, no 17, Art. no 17, 2020, doi: 10.7150/thno.44233.

[8] C. Demené et al., “Transcranial ultrafast ultrasound localization microscopy of brain vasculature in patients”, Nat Biomed Eng, vol. 5, no 3, p. 219-228, march 2021, doi: 10.1038/s41551-021-00697-x.

[9] N. Renaudin et al., “Functional ultrasound localization microscopy reveals brain-wide neurovascular activity on a microscopic scale”, Nat Methods, vol. 19, no 8, p. 1004-1012, aug. 2022, doi: 10.1038/s41592-022-01549-5.

[10] J. R. McCall et al. “Non-invasive transcranial volumetric ultrasound localization microscopy of the rat brain with continuous, high volume-rate acquisition”, vol.13, no 4, p. 1235-1246, Feb. 2023, doi: 10.7150/thno.79189 .

[11] J. R. McCall et al., “Longitudinal 3-D Visualization of Microvascular Disruption and Perfusion Changes in Mice During the Evolution of Glioblastoma Using Super-Resolution Ultrasound,” IEEE Transactions on Ultrasonics, Ferroelectrics, and Frequency Control, vol. 70, no. 11, pp. 1401-1416, Nov. 2023, doi: 10.1109/TUFFC.2023.3320034.

[12] K. M. Christensen-Jeffries, “Super-resolution ultrasound imaging with microbubbles”, PhD Thesis, King’s College London, 2017.

[13] K. Christensen-Jeffries et al., “Super-resolution Ultrasound Imaging”, Ultrasound in Medicine & Biology, vol. 46, no 4, Art. no 4, apr. 2020, doi: 10.1016/j.ultrasmedbio.2019.11.013.

[14] O. Couture et al., “Ultrasound Localization Microscopy and Super-Resolution: A State of the Art”, IEEE Trans. Ultrason., Ferroelect., Freq. Contr., vol. 65, no 8, p. 1304-1320, aug. 2018, doi: 10.1109/TUFFC.2018.2850811.

[15] O. Couture et al., “Microbubble ultrasound super-localization imaging (MUSLI)”, in Ultrasonics Symposium (IUS), 2011 IEEE International, IEEE, 2011, p. 1285-1287. doi: 10.1109/ULTSYM.2011.6293576.

[16] B. Heiles et al., “Ultrafast 3D Ultrasound Localization Microscopy Using a 32x32 Matrix Array”, IEEE Trans. Med. Imaging, vol. 38, no 9, Art. no 9, sept. 2019, doi: 10.1109/TMI.2018.2890358.

[17] O. Demeulenaere et al., “In vivo whole brain microvascular imaging in mice using transcranial 3D Ultrasound Localization Microscopy”, eBioMedicine, vol. 79, p. 103995, may 2022, doi: 10.1016/j.ebiom.2022.103995.

[18] B. Heiles et al., “Volumetric Ultrasound Localization Microscopy of the Whole Rat Brain Microvasculature”, IEEE Open J. Ultrason., Ferroelect., Freq. Contr., vol. 2, p. 261-282, 2022, doi: 10.1109/OJUFFC.2022.3214185.

[19] S. Harput et al., “3-D Super-Resolution Ultrasound Imaging With a 2-D Sparse Array”, IEEE Transactions on Ultrasonics, Ferroelectrics, and Frequency Control, vol. 67, no 2, Art. no 2, feb. 2020, doi: 10.1109/TUFFC.2019.2943646.

[20] A. Austeng et al., “Sparse 2-D arrays for 3-D phased array imaging - design methods”, IEEE Transactions on Ultrasonics, Ferroelectrics and Frequency Control, vol. 49, no 8, Art. no 8, aug. 2002, doi: 10.1109/TUFFC.2002.1026019.

[21] J. Sauvage et al., “A large aperture row column addressed probe for in vivo 4D ultrafast doppler ultrasound imaging”, Phys. Med. Biol., vol. 63, no 21, p. 215012, oct. 2018, doi: 10.1088/1361-6560/aae427.

[22] M. F. Rasmussen et al., “3-D imaging using row-column-addressed arrays with integrated apodization - part i: apodization design and line

element beamforming", IEEE Trans. Ultrason., Ferroelect., Freq. Contr., vol. 62, no 5, p. 947-958, 2015, doi: 10.1109/TUFFC.2014.006531.

[23] A. Chavignon et al., "3D Transcranial Ultrasound Localization Microscopy in the Rat Brain With a Multiplexed Matrix Probe", IEEE Trans. Biomed. Eng., vol. 69, no 7, p. 2132-2142, july 2022, doi: 10.1109/TBME.2021.3137265.

[24] A. Chavignon et al., "3D transcranial ultrasound localization microscopy for discrimination between ischemic and hemorrhagic stroke in early phase", Sci Rep, vol. 12, no 1, p. 14607, aug. 2022, doi: 10.1038/s41598-022-18025-x.

[25] Y. S. Ng et al., "Comparison of Clinical Characteristics and Functional Outcomes of Ischemic Stroke in Different Vascular Territories", Stroke, vol. 38, no 8, Art. no 8, aug. 2007, doi: 10.1161/STROKEAHA.106.475483.

[26] J.-H. Kwon et al., "The Thickness and Texture of Temporal Bone in Brain CT Predict Acoustic Window Failure of Transcranial Doppler", Journal of Neuroimaging, vol. 16, no 4, p. 347-352, oct. 2006, doi: 10.1111/j.1552-6569.2006.00064.x.

[27] A. D. Wijnhoud et al., "Inadequate Acoustical Temporal Bone Window in Patients with a Transient Ischemic Attack or Minor Stroke: Role of Skull Thickness and Bone Density", Ultrasound in Medicine & Biology, vol. 34, no 6, p. 923-929, june 2008, doi: 10.1016/j.ultrasmedbio.2007.11.022.

[28] R. S. C. Cobbold, Foundations of Biomedical Ultrasound, 1st ed. OUP USA, 2006.

[29] J. Provost et al., "3D ultrafast ultrasound imaging in vivo", Phys. Med. Biol., vol. 59, no 19, p. L1-L13, oct. 2014, doi: 10.1088/0031-9155/59/19/L1.

[30] V. Perrot et al., "So you think you can DAS? A viewpoint on delay-and-sum beamforming", Ultrasonics, vol. 111, p. 106309, march 2021, doi: 10.1016/j.ultras.2020.106309.

[31] J. A. Jensen, "A model for the propagation and scattering of ultrasound in tissue", The Journal of the Acoustical Society of America, vol. 89, no 1, Art. no 1, janv. 1991, doi: 10.1121/1.400497.

[32] J. A. Jensen, "Field: A Program for Simulating Ultrasound Systems", Medical & Biological Engineering & Computing, vol. 34, no Supplement 1, Part 1, p. 331-353, 1996.

[33] J. R. McCall et al. "Element Position Calibration for Matrix Array Transducers with Multiple Disjoint Piezoelectric Panels." Ultrasonic imaging,1617346241227900, Feb. 2024 ,doi:10.1177/01617346241227900